Final Draft
of the original manuscript:

Seydel, T.; Knoll, W.; Greving, I.; Dicko, C.; Koza, M.M.;
Krasnov, I.; Mueller, M.:

**Increased molecular mobility in humid silk fibers under
tensile stress**

Increased molecular mobility in humid silk fibers under tensile stress

Tilo Seydel,[1, *] Wiebke Knoll,[1, 2] Imke Greving,[3] Cedric
Dicko,[3] Michael M.Koza,[1] Igor Krasnov,[4] and Martin Müller[4, 5]

[1] *Institut Laue-Langevin, B.P.156, F-38042 Grenoble, France*
[2] *Université Joseph Fourier, Grenoble, France*
[3] *Department of Zoology, University of Oxford, OX13PS, U.K.*
[4] *IEAP, Universität Kiel, D-24098 Kiel, Germany*
[5] *Institute of Materials Research, GKSS, D-21502 Geesthacht, Germany*
(Dated: October 18, 2010)

Silk fibers are semi-crystalline nanocomposite protein fibers with an extraordinary mechanical toughness which changes with humidity. Diffusive or overdamped motion on a molecular level is absent in dry silkworm silk, but present in humid silk at ambient temperature. This microscopic diffusion distinctly depends on the externally applied macroscopic tensile force. Quasi-elastic and inelastic neutron scattering data as a function of humidity and of tensile strain on humid silk fibers support the model that both the adsorbed water and parts of the amorphous polymers participate in diffusive motion and are affected by the tensile force. Notably, the quasi-elastic linewidth of humid silk at 100% relative humidity increases significantly with the applied force. The effect of the tensile force is discussed in terms of an increasing alignment of the polymer chains in the amorphous fraction with increasing tensile stress which changes the geometrical restrictions of the diffusive motions.

I. INTRODUCTION

Silk belongs to a large class of polymer nanocomposite materials being of current fundamental and technological interest [1]. Silk fibers possess outstanding mechanical properties combining elasticity and tensile strength. Remarkably, these mechanical properties distinctly and reversibly change as a function of the humidity of the silk fibers [2–4]. In particular, the elasticity increases with humidity at the expense of the rupture strength. Humidity seems to decrease the glass transition temperature T_g in silk fibers, and a humidity-temperature T equivalence has been reported according to which the stress-strain curves follow a modulus-$(T_g - T)$ master curve [5]. The mechanical properties do not change linearly over the entire humidity range, but at least in the case of silkworm silk display a critical humidity at approximately 70% relative humidity (RH) above which the decay of the mechanical modulus with humidity is significantly enhanced [5]. Structural models for silk fibers have benefited from the rapid evolution of synchrotron x-ray microdiffraction techniques [6], nuclear magnetic resonance techniques [7], as well as since recently also neutron techniques [8]. Both silkworm silk and the morphologically similar spider silk are hierarchically structured protein polymers consisting of nanometer-sized Alanine-rich β-sheet crystallites embedded in an amorphous disordered Glycine-rich matrix. The silks differ predominantly in the volume fractions of the crystalline and amorphous parts [9, 10]. Silkworm silk and spider silk are also similar

in their mechanical properties [11]. In silkworm silk the volume fraction of the crystalline part is higher (approximately 60% [12]) compared to spider silk (approximately 30%). Viscoelastic models for the mechanical properties of silk fibers have been discussed for several years [13], and a strong interplay of morphology and the mechanical properties has been observed [14]. Most of the extensibility of the silk fibers can be attributed to the disordered phase whilst the crystallites are also elastically deformed [14]. The dynamical response of dry silkworm silk on a molecular level to an externally applied tensile force is in agreement with a model of entropy elasticity [15], which had already been proposed earlier for humid spider silk fibers [2]. Notably, relaxation processes on picosecond time scales, which are typical of water-plasticized polymers, are entirely absent in vacuum-dried silk fibers at ambient temperature [15].

With the present article, we report on a study of the dynamical response on a molecular level to an externally applied tensile force on humid silk fibers. Thus, we apply quasi-elastic (QENS) and low-energy inelastic (INS) neutron spectroscopy and we use water molecules as a spectroscopic probe to further understand the properties of silk fibers. Neutron spectroscopy accesses both spatial and time correlations by measuring the van Hove scattering function $S(Q,\omega)$ [16] depending on the scattering vector Q and the energy $\hbar\omega$. In the case of a biomaterial sample, the technique is predominantly sensitive to the single-particle correlation function of the hydrogen H-atoms through incoherent scattering. When the motion of these H-atoms is spatially restricted, information on the geometry of these spatial restrictions can be obtained [16]. It is already known from NMR studies [17] and also from neutron backscattering ex-

periments [8] on spider silk that water acts as a plasticizer to silk fibers. Quasi-elastic neutron spectroscopy has already previously been applied to related biopolymers such as hydrated collagen fibers [18], and a two-component model for the data analysis has been proposed discriminating scattering contributions from relatively freely diffusing hydration water and from strongly confined bound protons. We discuss our QENS data in terms of a model derived from Ref. [18] and related work. The choice of the model describing the QENS data from the hierarchically structured silk fibers is certainly not unique, and the effect of the parameters humidity and tensile force can only be analyzed quantitatively within a chosen model. Nevertheless, the significant increase of the quasi-elastic linewidth with increasing tensile strain in humid silk at 100% RH H_2O is model-independent. The results, although yet difficult to relate to common concepts in polymer science, have implications regarding the link between the macro state of fiber deformation and the polymer micro state.

We have used an experimental setup combining *in situ* hydration and *in situ* tensile testing with cold neutron time-of-flight spectroscopy on aligned silkworm silk fiber bundles. By applying the tensile force *in situ* on the spectrometer, a higher accuracy compared to a series of experiments on differently pre-stretched samples can be achieved. This is because by the *in situ* method any effect arising from different sample alignments can be excluded. Also, by applying an *in situ* humidification, a constant environmental humidity during tensile testing is guaranteed and any influence of unstable humidity conditions can be ruled out. In addition to the neutron time-of-flight data, we have recorded complementary neutron backscattering spectra on unstretched silk samples which were humidified *ex situ*. The backscattering data illustrate the plasticizing effect of water and its dependence on temperature.

A recent study addresses the effects of the tensile strain on the local order of *Bombyx mori* silkworm silk fibers at 65% RH H_2O using Raman scattering [19] and reports a reversible shift of several bands located above 800/cm towards lower wavenumbers with increasing tensile stress. Raman scattering is predominantly sensitive to the β-sheet crystallites [19]. By contrast, our quasi-elastic neutron scattering experiments are predominantly sensitive to the amorphous fraction of the silk which is accessible to the water molecules. In addition, we obtain low-energy inelastic data which provide information on both the crystalline and amorphous fractions.

II. EXPERIMENTAL

The silk samples have been obtained from *Bombyx mori* silk worms reared at the Department of Zoology, Oxford, U.K. The silk has been carefully degummed in 0.5 wt.% aqueous Na_2CO_3 solutions. Cold neutron spectroscopy experiments have been carried out at the high-

FIG. 1: (color) Photograph of a silk sample (white fiber bundle in the center of the image) inside the humidity chamber for *in situ* tensile testing mounted inside the sample bay of the time-of-flight spectrometer IN6. The chamber is shown with the front cover removed. The force sensor is visible as a cylindrical metal structure on the upper center of the photograph with the signal cable arriving from the right. The neutron beam impinges on the sample horizontally, arriving from the right edge of the photograph. The blue plastic troughs at the bottom of the chamber contain pure water or saturated salt solutions, respectively, to define the humidity inside the chamber. The edge-to-edge distance between the steel hooks holding the fiber bundle is 3 cm.

flux reactor of the Institut Laue-Langevin (ILL), Grenoble, France. The cross section of the beam impinging on the sample was approximately 3 cm high by 2 cm wide during all neutron experiments.

Backscattering experiments have been carried out using the instrument IN10 in the unpolished Si(111) monochromator and analyzer setup (wavelength 6.27Å, energy resolution 1μeV FWHM) on fiber bundles sealed in standard Aluminum sample holders without externally applied tensile strain (ILL experiment #8-04-423). The humidity of the single sample (dry mass (202 ± 1) mg)

used for the elastic window scans reported in this article was defined outside the spectrometer by storing the sample in atmospheres with different humidity defined by saturated salt solutions [20] and subsequently sealing the sample holder. The water uptake by this sample amounted to approximately 20% in mass after storage in 100% RH H_2O during 19 hours. The sealed sample was kept inside a standard Orange cryostat during the data acquisition to control the sample temperature.

Cold neutron time-of-flight (TOF) experiments have been carried out at the instrument IN6 (incident wavelength 5.1Å, elastic energy resolution $\approx 90\mu$eV FWHM) on vertically aligned fibers using a tensile machine with humidity chamber [21] (figure 1) at the temperature $T = (301 \pm 2)$ K mounted inside the spectrometer (ILL experiment #8-02-455). The humidity of the samples and the external tensile force were thus defined *in situ* without further manipulation of the sample between data acquisitions. The humidity was defined using pure water (H_2O and D_2O for 100% RH) and a saturated salt solution (NaCl in H_2O for 75% RH), respectively, placed in troughs inside the humidity chamber. Data on a dry sample were recorded at high vacuum to verify the reproducibility of the results for dry silk reported in Ref. [15]. The *in situ* tensile testing (figure 2) and humidification guarantees a constant environmental humidity and a constant sample alignment during stretching. This is important for the accuracy of the QENS data and the difference spectra discussed in this article. The humidity inside the chamber was measured using 2 capacitive humidity sensors located near the sample and near the troughs, respectively. The tensile force was measured using an Entran ELPM-T3M-2.5kN-/L3N sensor, and the temperature by a Pt100 sensor. The distance of the two parallel aluminum windows (thickness 1 mm each) for the neutrons was 10 mm, defining the path length of the neutron beam in the humid atmosphere (window plane at 135° relative to the incident beam axis), and the steel hooks carrying the silk sample were 5 mm high and 7.5 mm wide.

	humidities used	m_0/mg	n	A/mm^2
s1	dry & 75%RH H_2O	310.0 ± 0.1	19515	4.79
s2	100%RH H_2O&D_2O	190.6 ± 0.1	11847	2.91

TABLE I: Measured total dry mass m_0, calculated number of turns n around the steel hooks, and unstretched cross section area A for the two IN6 samples discussed in the present article.

The data were analyzed using standard *lamp* [22] macros for data reduction provided by the ILL Scientific Computing department and subsequently MATLAB 7.0.4.352, notably the MATLAB functions *lsqcurvefit* for fitting and *nlparci* for the optimization error estimation. All data have been normalized to the incident neutron flux and the relative detector efficiency obtained from the scattering signal of Vanadium plates placed at the sample position. The Vanadium plates were 0.25 mm
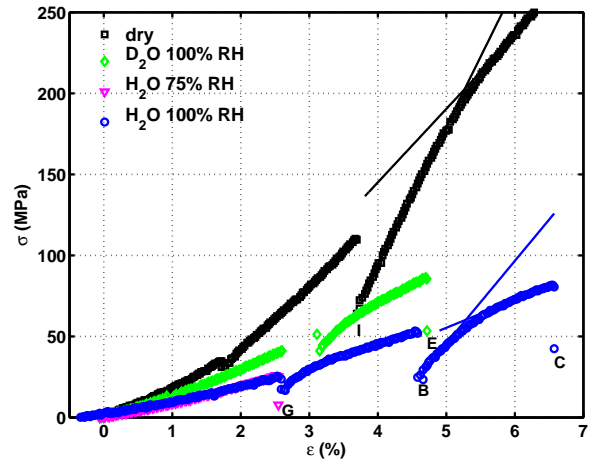

FIG. 2: Stress-strain curves obtained *in situ* during the IN6 experiment using the apparatus depicted in figure 1 (humidities see legend, sample properties table I). TOF data have been recorded at the positions on the stress-strain curves marked by the capital letters and at $\epsilon \approx 0$. The solid lines are linear fits to determine the mechanical moduli (see text).

thick and shaped to follow the sample geometry, three plates were stacked for the IN10 experiment, two plates – one plate on each side of the hooks of the tensile machine – were used on IN6. The empty can signal has been subtracted from all data presented in the following with the exception of Fourier transformed data. Intensities at equal in-plane scattering angle 2Θ have always been grouped. For the TOF spectra, the empty can and Vanadium signals were recorded on the tensile machine containing a saturated humid (H_2O) atmosphere. The TOF spectra have in addition been corrected for a constant background, the energy-dependence of the detector efficiency, and the frameoverlap background. *lamp* interpolation macros have been used to calculate the scattering function $S(Q,\omega)$ from the intensity data $I(2\Theta, t)$ recorded on IN6 as a function of the scattering angle 2Θ and neutron flight time t.

III. RESULTS AND DISCUSSION

A. *In situ* tensile testing

Stress-strain curves calculated from force-elongation curves recorded *in situ* during the IN6 experiment are depicted in figure 2 for dry silk and silk with different humidities, respectively. The stress σ is calculated from the measured force using the total effective cross section area A (table I) of the respective fiber bundle. A is calculated from microscope optical measurements of single fiber diameters d and the mass density $\rho = 1.38$ kg/m^3 [23] of *Bombyx mori* fibers. We have obtained the average $d = (12.5 \pm 2.5)\mu$m. The strain ϵ is calculated using the measured elongation and an additional offset which

takes into account that the fibers initially slide around the hooks without actually being strained. The offset is obtained by a linear fit to the lowest linear range of the force-elongation curve. The neutron spectra have been recorded at approximately 0 strain as soon as a full parallel alignment of the fibers in the bundle sample was reached, and at the positions marked by the letters in figure 2. The force-elongation curves were always recorded at a constant elongation rate of $0.04\,\mathrm{mm/s}$, resulting in the strain rate $\dot{\epsilon} \approx 0.08\,\%/\mathrm{s}$. The discontinuities in the stress-strain curves at the positions where neutron spectra were recorded arise from the fact that when the continuous fiber extension is stopped, a relaxation process in the silk fibers occurs on a time scale of a few minutes resulting in a reduction of the measured tensile stress [14]. This relaxation can be neglected in the neutron data analysis, since the acquisition time for the neutron spectra is on the order of several hours. From the slopes of the stress-strain curves immediately following the neutron data acquisition and far above, respectively, we can estimate the modulus $G_g = G + G_e$ of the silk in terms of the 3-parameter Maxwell model [14], where G_e is the elastic and G is the relaxation modulus. We obtain from linear fits (lines in figure 2) $G = 1.02\,\mathrm{GPa}$, $G_e = 480\,\mathrm{MPa}$ for dry silk, and $G = 605\,\mathrm{MPa}$, $G_e = 399\,\mathrm{MPa}$ for 100% RH H_2O humid silk, respectively. These values are by a factor 5 to 10 smaller than literature values obtained on single fibers [24]. We explain this discrepancy by the large fiber bundles which we used for the neutron experiment and by the large natural variability in the mechanical properties [23].

B. Neutron backscattering elastic window scans

Using the backscattering spectrometer IN10, we have recorded the elastic scattering from one silk sample as a function of temperature at different humidities. This scattering signal is elastic within the extremely high energy resolution of $1\mu\mathrm{eV}$ FWHM. The total elastic signal (figure 3, main part) can be attributed to the hydrogen atoms which are immobile on the instrumental resolution time scale of a few nanoseconds. The weaker elastic scattering intensity of humid silk compared to dry silk at room temperature corroborates the assumption that not only the adsorbed water molecules but also parts of the silk are mobile in humid silk. This reasoning is based the observation that the total number of scattering atoms in the humid silk samples is higher than in the dry silk sample – the water has been added to the same sample –, but nevertheless the total signal from immobile atoms is lower. The fact that the added water actually contributes to the total scattering intensity can be verified from the elastic intensities recorded at the lowest temperatures. This is also in reasonable agreement with the water uptake in mass at 100% RH (section II).

From the dependence of the elastic signal on the scattering vector Q, we can determine the thermal Debye-
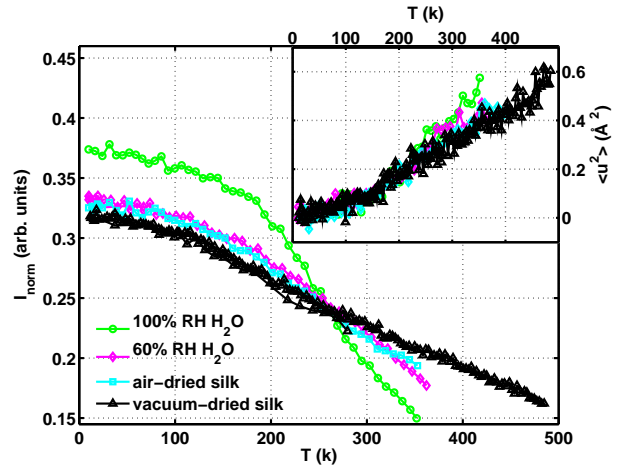

FIG. 3: Elastic scattering intensities recorded on IN10 within the $1\,\mu\mathrm{eV}$ resolution window, integrated over all detectors. All data have been taken on the same silk sample, and the differences in the intensities at the lowest temperature are therefore a measure of the water contents. Inset: Mean-squared displacements $\langle u^2 \rangle$ calculated from the Q-dependence of the intensities $I(Q)$ according to $I(Q) \propto \exp\left(-\frac{1}{3}\langle u^2 \rangle Q^2\right)$.

Waller factor [25]. The resulting mean-squared displacement $\langle u^2 \rangle$ is linear in the temperature T for $T > 100\,\mathrm{K}$ for dry silk (inset of figure 3). This is reminiscent of a harmonic solid. With increasing humidity, a deviation from this linear dependence seems to occur at temperatures above approximately $200\,\mathrm{K}$ which is consistent with the plasticizing effect of the adsorbed water generally observed for humid proteins [26]. In this case $\langle u^2 \rangle$ in $I(Q) \propto \exp\left(-\frac{1}{3}\langle u^2 \rangle Q^2\right)$ is only an "apparent" displacement due to the underlying quasi-elastic signal.

We have also recorded backscattering spectra as a function of the energy transfer $-10\mu\mathrm{eV} \leq E \leq +10\mu\mathrm{eV}$ giving access to the quasi-elastic scattering from nanosecond relaxations. These spectra indicate the presence of a minute quasi-elastic signal in humid silk which is too weak for a quantitative analysis (not shown) and a complete absence of such a signal in dry silk. Therefore, most of the existing diffusive motion in humid silk seems to take place on faster (picosecond) time scales.

C. Neutron time-of-flight spectra

Whilst the cold neutron backscattering data discussed in the previous subsection address the elastic and nanosecond quasi-elastic signals, the cold neutron time-of-flight spectra give access to picosecond and faster time scales, as explained in the following. From the TOF spectra recorded on the instrument IN6, we derive four types of information: (1) From the diffraction data contained in the TOF spectra we obtain structural information, in particular regarding the β-sheet correlation peak near $1.4\,\text{Å}^{-1}$. (2) From the ratio of the elastic and
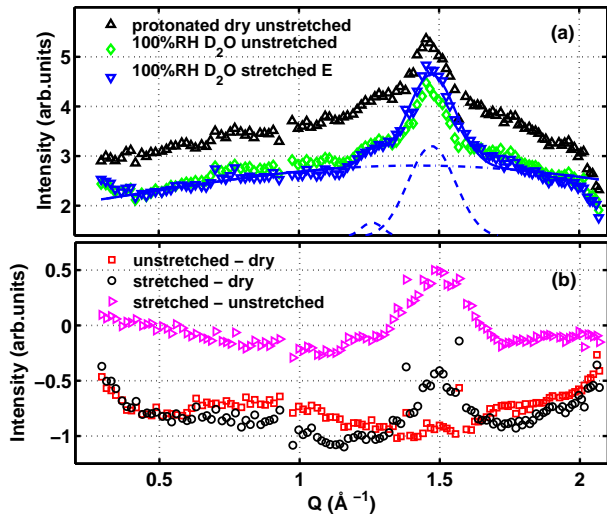
FIG. 4: (a) Diffraction patterns recorded on IN6 on dry and 100% RH D_2O-humid silk (symbols). The scattering intensities have been normalized taking into account the different illuminated masses. The label "E" refers to the stress-strain curve (Fig. 2). The solid line is a fit of a sum of three Gaussians, denoted by dashed and dash-dotted lines, respectively, to the D_2O-humid stretched silk. (b) Difference patterns from (a) as specified in the legend. The labels "stretched" and "unstretched" both denote 100% D_2O-humid silk.

quasi-elastic scattering we obtain the elastic incoherent structure factor which can be interpreted in terms of geometrical models of steric restriction of diffusion processes in the silk. (3) From the low-energy inelastic data we derive the generalized frequency distribution. (4) From the quasi-elastic data we obtain diffusion constants and frequencies of the overdamped motions in the system.

(1) The sum of the TOF spectra over the TOF channels near the elastic line results in the diffraction pattern of the sample (symbols in figure 4(a)). The poly(alanine) (110) and (020) peaks rise above the amorphous halo (broad Gaussian denoted by the dash-dotted line in figure 4(a)) [27] and can be identified and located by a fit (dashed lines in figure 4(a)) at $1.47\,\text{Å}^{-1}$ and $1.26\,\text{Å}^{-1}$, respectively, in good agreement with previous diffraction data [8, 15, 27]. The addition of D_2O leads to an H/D exchange. Therefore, the patterns from the humid sample are lower in intensity than the patterns from the dry sample. At $Q > 2\,\text{Å}^{-1}$, an increased absorption in the plane of the silk fibers and humidity chamber windows obscures the signal. We note that further geometrical effects may influence the scattering, which are difficult to model for our complex sample environment. We observe that the stretching leads to a better contrast between crystalline and amorphous regions in humid silk with the (poly)alanine peak becoming stronger. We attribute this to a better alignment of the crystallites upon stretching. This is emphasized in the difference pattern "stretched - unstretched" where a maximum near $1.5\,\text{Å}^{-1}$ remains (figure 4(b)). The absence of an H/D exchange
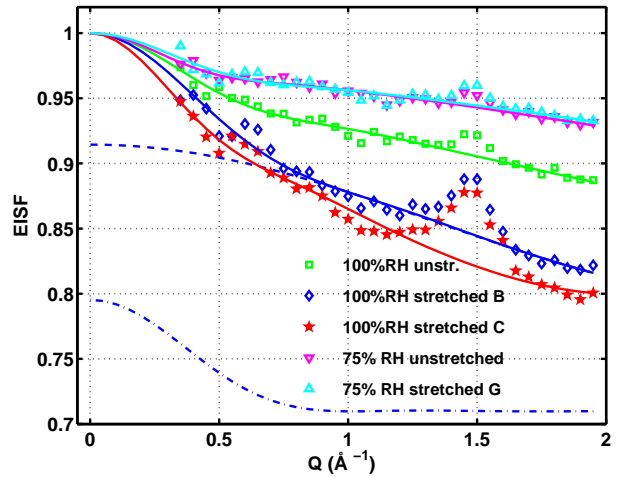

FIG. 5: Elastic incoherent structure factors (symbols) of H_2O-humid silk (100% RH and 75% RH, respectively), calculated from $S(Q,\omega)$-data grouped in Q. The solid lines denote fits according to eq. 2. The dashed and dash-dotted lines indicate the two-site jump and diffusion inside a sphere contributions, respectively, for the silk stretched to position B in figure 2. The poly-alanine peak near $1.4\,\text{Å}^{-1}$ (figure 4) has been excluded from the fit. In eq. 3, $p = 0.5$ has been fixed. The humid silk EISFs have been normalized by the dry silk EISF. The fit parameters are summarized in table II.

	100% RH unstretched	100% RH stretch B	100% RH stretch C	75% RH unstretched
Φ	0.74 ± 0.13	0.71 ± 0.07	0.75 ± 0.06	0.81 ± 0.25
$a[\text{Å}]$	1.33 ± 0.93	1.55 ± 1.04	2.12 ± 0.31	1.06 ± 1.21
$R[\text{Å}]$	5.07 ± 0.74	4.43 ± 0.83	5.97 ± 1.26	6.34 ± 1.20
c_0	0.79 ± 0.14	0.71 ± 0.13	0.72 ± 0.02	0.83 ± 0.24

TABLE II: Fit results to the EISF (figure 5) according to equation 2 for 100% RH H_2O humid silk unstretched and stretched B and C (referring to the labels in figure 2), and 75% RH H_2O humid silk unstretched, respectively. The optimization errors are given within 95% confidence limits.

in the crystalline parts is confirmed by the difference "unstretched - dry".

(2) From the elastic incoherent structure factor (EISF), parameters associated with the geometry of confinement of diffusing molecules can be derived [16]. From our IN6 data, we approximate the elastic incoherent structure factor (figure 5) by [28]

$$A(Q) := \text{EISF}(Q) = \frac{\int_{-70\mu\text{eV}}^{+70\mu\text{eV}} S(Q,\omega)\,d\omega}{\int_{-0.53\text{meV}}^{+0.53\text{meV}} S(Q,\omega)\,d\omega}. \quad (1)$$

The denominator approximately covers the QENS region without integrating over too much of the inelastic region. The integration range over the elastic peak covers approximately 1.5 times the weakly Q-dependent resolution FHWM.

A large number of models have been elaborated to de-

scribe different geometries of confinement and the resulting EISFs [16]. The problem to decide for a particular model from our EISF data alone is ill-posed, but we conclude from the double slope change in the EISFs from 100% RH H_2O humid silk that two characteristic length scales of confined diffusion are present. As the simplest model, following Bicout [29] we fit

$$A(Q) = (1-c_0)\,(\Phi A_{\text{jump}}(Q) + (1-\Phi)A_{\text{sphere}}(Q)) + c_0 \quad (2)$$

to the humid silk data with the volume fraction Φ undergoing jump diffusion between two sites separated by the distance or jump length a,

$$A_{\text{jump}}(Q) = 1 - 2p[1 - j_0(Qa)], \quad (3)$$

and the volume fraction Φ undergoing diffusion inside a sphere with radius R,

$$A_{\text{sphere}}(Q) = \left| \frac{3j_1(QR)}{QR} \right|^2. \quad (4)$$

Therein, $j_l(x)$ is the spherical Bessel function of the first kind and order l. c_0 quantifies the constant elastic contribution of the scatterers not undergoing any diffusion. p is the probability to locate the jump-diffusing particle on one out of two sites. The additive model (equation 2) is reasonable, because the system consisting of amorphous polymer chains and adsorbed water can be assumed to be dynamically heterogeneous [29]. The model has been proposed for hydrated protein systems to describe the fluctuations of the protein backbone [30]. We assume that the protein and strongly bound water contributions are accounted for by this model. An additional component of unrestricted jump diffusion of weakly bound water, which we assume for the QENS fit, has 0 numerator in eq. 1. The sharper correlation peak near $1.4\,\text{Å}^{-1}$ for stretched silk is attributed to the better alignment of the crystallites under tensile stress (figure 4). This coherent scattering contribution has been excluded from the fit to the EISF.

The EISF fit results are summarized in table II. The result for Φ indicates a predominant two-site jump diffusion, but also a clear presence of diffusion inside a sphere. We observe a trend towards an increase of the two-site jump distance with the tensile strain in humid silk. This can be associated with the better alignment of the amorphous polymer chains. The fit results for the unstretched silk at 100% and 75% relative humidity, respectively, are reasonable in comparison. Thus, more adsorbed water results in a smaller value for the immobile fraction c_0.

(3) The time-of-flight spectra contain information on the low-energy inelastic scattering up to on the order of 100 meV on the neutron energy gain side of the spectrum. In this region, the water translation and libration modes as well as some signals from the crystallites of the silk can be observed. For a quantitative analysis, we derive the Q-integrated generalized frequency distribution $P(\beta) = \int_\alpha P(\alpha, \beta)$ according to [31]

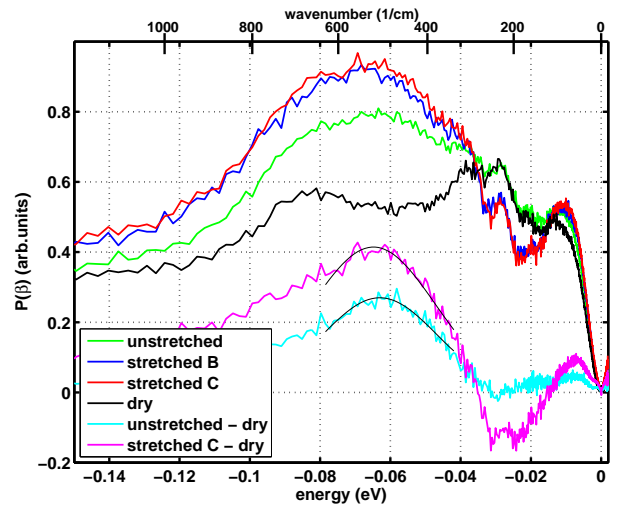$$P(\alpha, \beta) = 2\beta \sinh(\beta/2) \frac{\tilde{S}(\alpha, \beta)}{\alpha} \quad (5)$$

FIG. 6: Q-integrated generalized frequency distribution calculated from the time-of-flight spectra on dry and humid samples at 100% RH H_2O, respectively. The thin black lines superimposed on the difference spectra "humid - dry" are indicative fits of a Gaussian line shape to determine the position of the maximum of the water librational peak. The capital letters in the legend refer to the positions on the stress strain curves marked in figure 2. The TOF-spectra have been normalized to equal total intensity for accurate comparison.
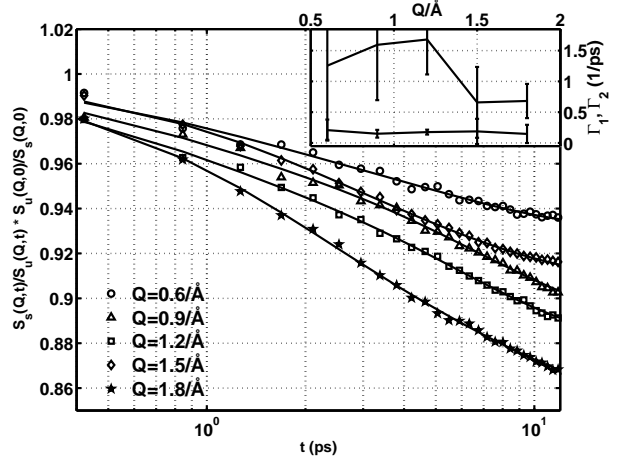

FIG. 7: Ratio of the intermediate scattering functions $S_s(Q,t)$ from the 100% RH H_2O-humid silk stretched to position C (figure 2) and $S_u(Q,t)$ from unstretched 100% RH H_2O-humid silk obtained from a Fourier transform of the data recorded on IN6 (symbols). The lines are fits of $S_s(t)/S_u(t) = I_1 \exp(-\Gamma_1 t) + I_2 \exp(-\Gamma_2 t)$. Inset: Fit results for Γ_1 and Γ_2. The error bars denote 95% confidence limits of the fit.

from the scattering function $\tilde{S}$ in the reduced coordinates

$$\alpha = \frac{\hbar^2 Q^2}{2Mk_BT} \quad \text{and} \quad \beta = \frac{\hbar^2 \omega}{k_BT} \quad (6)$$

with the atom mass M.

The generalized frequency distribution (figure 6) reveals the water libration peak maximum in humid silk

near $-64\,\text{meV}$. The low-frequency water librations are sensitive to localized hydrogen bonding and steric restrictions [32]. In our silk data we observe that the water libration peak shifts from approximately $-63\,\text{meV}$ in the unstretched case to $-65\,\text{meV}$ for the stretched sample. A shift of the libration peak to higher absolute values indicates a stronger confinement [33]. The peak at $-28\,\text{meV}$ has been tentatively assigned to a vibrational mode of the crystallites [15], since it corresponds to a minimum in the protonated - deuterated dry silk difference spectra. The strong effect of stretching in this region is in agreement with the better alignment of the crystallites under strain. The vanishing of the peak at $-28\,\text{meV}$ in the difference spectra humid - dry corroborates the assumption that this peak arises from the crystallites which are not accessible to water [15]. Besides the crystalline peak, the region between -20 and $-30\,\text{meV}$ is dominated by hydrogen translations [32]. Interestingly, in this region the difference (humid stretched) - (dry) is negative. This is consistent with the hypothesis that not only the water itself is affected by a change of the vibrational density of states in humid silk, but also the silk polymer chains (see the discussion along figure 3).

(4) As stated in the introduction, with the present data and knowledge we cannot yet elaborate a model which unambiguously describes the quasi-elastic signal from the hierarchically structured silk. Due to the accuracy of the *in situ* method a model-free comparison of the intermediate scattering functions $S_s(Q,t)$ from stretched and $S_u(Q,t)$ from unstretched H_2O-humid silk is nevertheless possible (figure 7). Here, $S_u(Q,t)$ serves as "resolution" function, and the ratio $S_s(Q,t)/S_u(Q,t)$ reveals those dynamical processes which are affected by the tensile strain. $S_s(Q,t)/S_u(Q,t)$ can be well described by a sum of two exponentials. This suggests that at least two distinct diffusion processes are affected by the strain. We carry out a more detailed model fitting in the energy rather than in the time domain in the following.

For the interpretation of the QENS data (figure 8) we apply the same additive model describing the dynamically heterogenous silk as assumed for the fit to the EISF. Since a component of unrestricted translational jump diffusion would not or nearly not contribute to the EISF, we have to add this component to the model describing the QENS signal. The hypothesis of this additional component is in line with the evident, however weak, presence of a Q-dependent linewidth in the QENS data from humid silk. Thus, we assume a dynamical population c_j undergoing unrestricted jump diffusion. The remaining $(1-c_j)$ of scatterers is composed of a population Φ that undergoes two-site jump diffusion between sites with distance a, and a population $(1-\Phi)$ that diffuses inside a sphere with radius R [16, 34, 35]:

$$
\begin{aligned}
S_{\text{QENS}}(Q,\omega) = \quad & (1-c_j)\left\{(1-\Phi)\left[\left(\tfrac{3j_1(QR)}{QR}\right)^2\delta(\omega) + \left(1-\left(\tfrac{3j_1(QR)}{QR}\right)^2\right)\tfrac{1}{\pi}\tfrac{\Gamma}{\Gamma^2+\omega^2}\right]\right. \\
& \left. + \Phi\left[\tfrac{1}{2}(1+j_0(Qa))\delta(\omega) + \left(\tfrac{1}{2}(1-j_0(Qa))\tfrac{1}{\pi}\tfrac{2\tau}{4+\tau^2\omega^2}\right)\right]\right\} + c_j\left(\tfrac{1}{\pi}\tfrac{\Gamma_u(Q)}{\Gamma_u^2(Q)+\omega^2}\right)
\end{aligned} \tag{7}
$$

Therein, Γ is the linewidth due to the diffusion inside a sphere, τ is the residence time between two-site jumps, $j_l(x)$ is the spherical Bessel function of first first kind and order l, and

$$
\Gamma_u(Q) = \frac{DQ^2}{1+DQ^2\tau_0} \tag{8}
$$

is the linewidth due to unrestricted jump diffusion with the diffusion constant D and residence time τ_0. To this we add the contribution $S_{\text{elastic}}(Q,\omega) = \exp\left(-WQ^2\right)\delta(\omega)$ with $\int_{-\infty}^{\infty}\exp\left(-WQ^2\right)\delta(\omega)\,d\omega = c_0$ and the Debye-Waller factor W such that

$$
\int_{-\infty}^{\infty} S(Q,\omega)\,d\omega =
$$
$$
\int_{-\infty}^{\infty}\left[c_{\text{QENS}}\,S_{\text{QENS}}(Q,\omega) + S_{\text{elastic}}(Q,\omega)\right]d\omega
$$
$$
= c_{\text{QENS}}\int_{-\infty}^{\infty} S_{\text{QENS}}(Q,\omega)\,d\omega + c_0 = 1. \tag{9}
$$

Therein, c_{QENS} and c_0 scale the magnitudes of the fractions contributing to the quasi-elastic and elastic signals, respectively. We fix c_0, a, R, and Φ in equation 7 using the results from the fits to the EISF (figure 5, table II) according to eq. 2. Furthermore, we fix $W = \tfrac{1}{3}\,0.36\,\text{Å}^2$ from the result for the mean-squared displacement for dry silk (inset of figure 3), thereby assuming that the additional contribution to the apparent $\langle u^2\rangle$ in humid silk is only due to diffusion. Using these assumptions, we obtain the results summarized in table III from fitting $S(Q,\omega)$ (eq. 9) convoluted with the spectrometer resolution function to the QENS data. The resulting fits are displayed in figure 8. As spectrometer resolution we use the unstretched dry silk data rather than the Vanadium, because no quasi-elastic broadening is present in dry silk [15], and any influence of a different alignment of the resolution sample can is this way be ruled out. We use the resolution data directly without an analytical approximation. We fit five groups in Q simultaneously, i.e. we do not allow for an individual amplitude scaling of
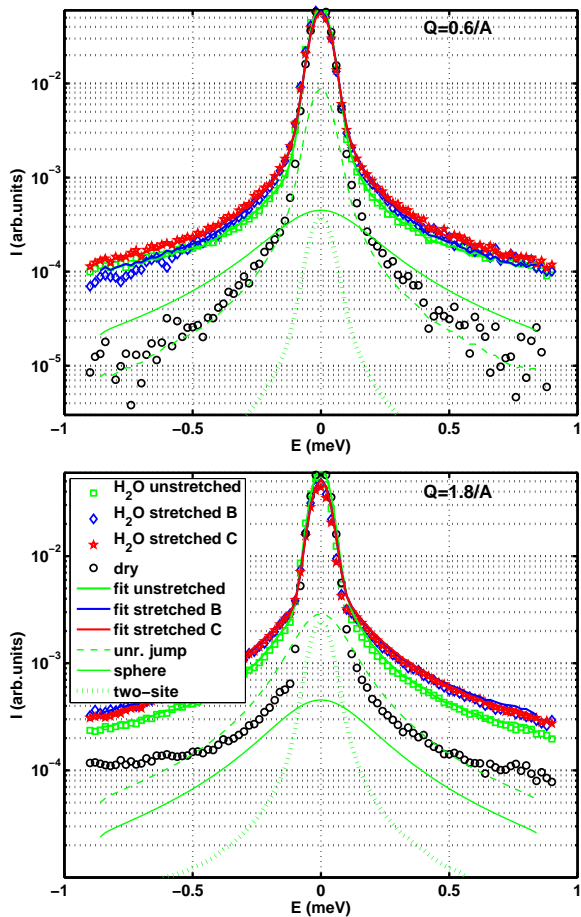
FIG. 8: QENS data (symbols) from 100% RH H_2O humid silk and dry silk, respectively. The thick solid lines are fits of eq. 9 simultaneously to all 5 Q-groups – out of which only two are shown – after convolution with the dry silk data which have been assumed as resolution function. The dashed lines indicate the contributions of unrestricted jump diffusion, the dash-dotted lines represent the two-site jump diffusion, and the thin solid lines mark the diffusion on a sphere, respectively, for the example of the unstretched 100% RH H_2O-humid silk. All fit components are shown after convolution with the instrument resolution. The Q-dependence of eq. 9 has been imposed on the fit.

	unstretched	stretch B	stretch C
$D[10^{-5}\mathrm{cm}^2/\mathrm{s}]$	0.59 ± 0.12	0.88 ± 0.16	1.37 ± 0.16
$\tau_0[10^{-12}\mathrm{s}]$	1.53 ± 1.37	0.49 ± 0.88	2.27 ± 0.49
$\Gamma[10^{11}\mathrm{Hz}]$	2.94 ± 0.38	1.89 ± 0.37	3.10 ± 1.00
$\tau[10^{-12}\mathrm{s}]$	93.52 ± 157.34	1.09 ± 0.38	4.01 ± 1.20
c_j	0.48 ± 0.03	0.43 ± 0.03	0.64 ± 0.04
c_0 (fixed)	0.790	0.710	0.720
Φ (fixed)	0.740	0.710	0.750
$a[\text{Å}]$ (fixed)	1.330	1.550	2.120
$R[\text{Å}]$ (fixed)	5.070	4.430	5.970
$3W[\text{Å}^2]$ (fixed)	0.360	0.360	0.360
$\Gamma R^2/4.33[\mathrm{cm}^2/\mathrm{s}]$	1.745E-04	8.552E-05	2.551E-04

TABLE III: Fit results according to equation 7 for 100% RH H_2O-humid silk unstretched and stretched to positions B and C (labels in figure 2), respectively (see figure 8). The optimization errors are given within 95% confidence limits. The values for Φ, a, R, and c_0 have been obtained from the fit to the EISF (figure 5), the value for W from the mean-squared displacement (figure 3). $\Gamma R^2/4.33$ is the apparent diffusion constant of the diffusion inside a sphere [35].

D. Further discussion of the EISF and QENS fits

We emphasize that the choice of the model in terms of which we discuss our data is not unique. The most robust observations are the presence of at least two length scales of confined diffusion, namely a and R, which can be identified in the EISF (figure 5), and the overall quasi-elastic linewidth (figure 8). The latter significantly changes with increasing tensile strain on the humid fibers at 100% RH humidity H_2O. In addition, the Fourier transform suggests that two distinct time scales of diffusive motion are affected by the tensile strain in 100% RH H_2O-humid silk (figure 7). By comparing the fits in the time domain and in the energy domain, the low-frequency process $\Gamma \approx 0.1$ THz (inset of figure 7) corresponds by order of magnitude to the change of the unrestricted jump diffusion constant D (table III). The high-frequency process $\Gamma \approx 1$ THz (inset of figure 7) can tentatively be associated with the two-site jumps, whilst the nearly strain-independent relaxation due to the diffusion inside a sphere does not appear in the ratio $S_s(Q,t)/S_u(Q,t)$.

We associate the unrestricted jump diffusion with weakly bound adsorbed water molecules. These water molecules contribute only a fraction to the total QENS scattering signal, which supports the assumption that not only weakly bound water undergoes diffusive motion in humid silk. The unrestricted jump diffusion coefficient D is significantly smaller than the bulk water jump diffusion coefficient $D_{H_2O,\text{bulk}} = 2.5 \cdot 10^{-5}$ cm^2/s [36], indicating that the water molecules remain at least weakly bound even in stretched fibers. Concluding from the fit values for D, the weakly bound water becomes faster when the fibers are stretched. We assign the two-site jumps to polymer side groups, predominantly those of

the groups. We only allow for a constant Q-dependent background, which turns out to be negligible. For fitting $S(Q,\omega)$ we cannot use as many groups in Q as for the fit to the EISF due to the insufficiently strong signal. The parameters c_{QENS} and c_0 are connected through $c_{\text{QENS}} = 1 - c_0$. Technically, c_{QENS} is a fit parameter constrained by the condition $\int S(Q,\omega)\,d\omega = 1$ (eq. 9). We have neglected the rotational diffusion component of the adsorbed water because it cannot be determined independently in the absence of low-temperature QENS data [36]. The rotational diffusion contributes a small constant offset to the translational diffusion constant [36].

glycine. The diffusion inside a sphere may be both due to strongly bound water molecules [37] and due to polymer side groups. The fit to the EISF indicates that the diffusing protons not belonging to unrestricted water mostly contribute with a fraction Φ to the two-site jumps of the polymer side groups. This further supports the assumption that not only the water molecules themselves, but also the amorphous silk polymer chains contribute to the diffusion processes. The fit parameters we obtain are reasonable in the context of hydrated protein systems (see e.g. Ref. [38] and references therein). In particular, the diffusion constants D are reasonably near typical values found for protein hydration water [39]. The apparent diffusion coefficient of the diffusion on a sphere [35] $\Gamma R^2/4.33$ is by a factor of 5 to 10 larger than typical values found for hydration water of globular proteins [40]. This corroborates the hypothesis that predominantly the water-fluidified polymer side groups and not the water molecules undergo this type of diffusion.

IV. CONCLUSIONS AND OUTLOOK

Humid silk fibers are mechanically significantly different from dry silk fibers. Our neutron spectroscopy data support the model that the presence of water fluidifies the amorphous polymer fraction in the silk fibers such that both the water and the amorphous polymer chains display a diffusive mobility in humid fibers. This diffusive mobility is entirely absent in dry silk fibers. In the presence of water (H_2O) adsorbed to silk fibers at 100% RH, we also observe a strong effect of an externally applied macroscopic tensile strain on the microscopic molecular mobility within the amorphous fraction of the silk polymer fibers. This effect is equally absent in dry fibers. The width of the picosecond quasi-elastic signal perpendicular to the fiber axis in the 100%RH humid silk increases with the externally applied tensile force. This indicates a reduction of the viscous damping within the amorphous regions under strain which can be interpreted in the picture of a better alignment of the amorphous chains. In addition, the low-energy inelastic scattering is affected by the tensile strain in humid silk.

From the quantitative analysis of the QENS signal we conclude that in 100% RH humid silk the diffusion constant of the weakly bound adsorbed water and the molecular jump distance assigned to the amorphous polymers increase with the tensile strain. The adsorbed water and the exchangeable hydrogens in the amorphous regions of the silk fibers seem to contribute to the scattering signal associated with the strain-dependent mobility. We attribute this change in the mobility to the change of the geometry to which the water and H/D-exchangeable polymer side groups are confined in agreement with a better alignment of the amorphous chains.

We speculate that the tensile strain has a similar effect as the humidity on the glass transition temperature T_g [5]. In this picture, an increasing tensile strain would decrease T_g and thus explain the faster diffusive mobility. To verify this, a temperature-dependent humidity-controlled tensile experiment would be required, which is at present not achievable. Our tensile experiments thus far have been carried out with the neutron scattering plane being perpendicular to the silk fiber axis. Experiments with the silk fibers being in the scattering plane will have to be complemented to investigate any possible anisotropy. These experiments will be technically even more challenging, because a tensile apparatus with the tensile force being in-plane cannot be easily implemented. Furthermore, experiments with a significantly increased neutron flux would help to improve the modeling of the data. This may be envisioned at future neutron sources.

[1] D. Gersappe, Phys.Rev.Lett. **89**, 058301 (2002).

[2] J. Gosline, M. Denny, and M. Demont, Nature **309**, 551 (1984).

[3] J. Perez-Rigueiro, C. Viney, J. Llorca, and M. Elices, Polymer **41**, 8433 (2000).

[4] J. Perez-Rigueiro, C. Viney, J. Llorca, and M. Elices, Journal of Applied Polymer Science **75**, 1270 (2000).

[5] C. Fu, D. Porter, and Z. Shao, Macromolecules **42**, 7877 (2009).

[6] C. Riekel, M. Gutierrez, A. Gourrier, and S. Roth, Analytical and Bioanalytical Chemistry **376**, 594 (2003).

[7] G. Holland, R. Lewis, and J. Yarger, Journal of the American Chemical Society **126**, 5867 (2004).

[8] D. Sapede, T. Seydel, V. Forsyth, M. Koza, R. Schweins, F. Vollrath, and C. Riekel, Macromolecules **38**, 8447 (2005).

[9] Y. Shen, M. Johnson, and D. Martin, Macromolecules **31**, 8857 (1998).

[10] O. Hakimi, D. P. Knight, M. M. Knight, M. F. Grahn, and P. Vadgama, Biomacromolecules **7**, 2901 (2006).

[11] Z. Shao and F. Vollrath, Nature **418**, 741 (2002).

[12] G. Freddi and M. Tsukada, in *Polymeric Material Encyclopedia*, edited by J. Salmone (CRC Press: Boca Raton, FL, 1996), pp. 7734–7744, Vol.10.

[13] Y. Termonia, Macromolecules **27**, 7378 (1994).

[14] I. Krasnov, I. Diddens, N. Hauptmann, G. Helms, M. Ogurreck, T. Seydel, S. S. Funari, and M. Müller, Phys.Rev.Lett. **100**, 048104 (2008).

[15] T. Seydel, K. Kölln, I. Krasnov, I. Diddens, N. Hauptmann, G. Helms, M. Ogurreck, S.-G. Kang, M. M. Koza, and M. Müller, Macromolecules **40**, 1035 (2007).

[16] M. Bée, *Quasielastic neutron scattering. Principles and applications in solid state chemistry, biology and materials science* (A. Hilger, Bristol and Philadelphia, 1988).

[17] G. P. Holland, J. E. Jenkins, M. S. Creager, R. V. Lewis, and J. L. Yarger, Biomacromolecules **9**, 651 (2008).

[18] H. D. Middendorf, A. Traore, L. Foucat, J. P. Renou, and M. Ferrand, Physica B: Condensed Matter **276-278**, 518 (2000).

[19] T. Lefèvre, F. Paquet-Mercier, S. Lesage, M.-E. Rousseau, S. Bédard, and M. Pézolet, Vibrational Spectroscopy **51**, 136 (2009).

[20] F. E. M. O'Brien, Journal of Scientific Instruments **25**, 73 (1948).

[21] W. Knoll, *Neutron scattering experiments on silk fibers*, IEAP, University of Kiel, Germany (2008), Diploma thesis.

[22] D. Richard, M. Ferrand, and G. J. Kearley, *The Lamp Book*, Institut Laue-Langevin, Grenoble, France (2010).

[23] H.-P. Zhao, X.-Q. Feng, and H.-J. Shi, Materials Science and Engineering: C **27**, 675 (2007).

[24] J. Perez-Rigueiro, C. Viney, J. Llorca, and M. Elices, Journal of Applied Polymer Science **70**, 2439 (1998).

[25] W. Doster, S. Cusack, and W. Petry, Nature **337**, 754 (1989).

[26] M. T. F. Telling, C. Neylon, S. H. Kilcoyne, and V. Arrighi, J.Phys.Chem. B **112**, 10873 (2008).

[27] D. T. Grubb and L. W. Jelinski, Macromolecules **30**, 2860 (1997).

[28] M. Bee, Physica B **182**, 323 (1992).

[29] D. Bicout, Proceedings of the ILL millennium symposium and european user meeting **1**, 60 (2001).

[30] D. J. Bicout, Phys. Rev. E **64**, 011910 (2001).

[31] A. Fontana, F. Rocca, M. P. Fontana, B. Rosi, and A. J. Dianoux, Phys. Rev. B **41**, 3778 (1990).

[32] N. W. Ockwig, R. T. Cygan, M. A. Hartl, L. L. Daemen, and T. M. Nenoff, Journal of Physical Chemistry C **112**, 13629 (2008).

[33] V. Crupi, D. Majolino, P. Migliardo, and V. Venuti, J.Phys.Chem. A **104**, 11000 (2000).

[34] F. Gabel and M.-C. Bellissent-Funel, Biophysical Journal **92**, 4054 (2007).

[35] F. Volino and A. J. Dianoux, Molecular Physics **41**, 271 (1980).

[36] J. Teixeira, M.-C. Bellissent-Funel, S. H. Chen, and A. J. Dianoux, Phys. Rev. A **31**, 1913 (1985).

[37] M.-C. Bellissent-Funel, J. Teixeira, K. Bradley, and S. H. Chen, J. Phys. I France **2**, 995 (1992).

[38] M.-C. Bellissent-Funel, European Physical Journal E **12**, 83 (2003).

[39] M.-C. Bellissent-Funel, Faraday Discussions **103**, 281 (1996).

[40] J.-M. Zanotti, M.-C. Bellissent-Funel, and J. Parello, Biophysical Journal **76**, 2390 (1999).